GMR
The Original

ANN-GUIDED SYNTHESIS OF BACTERIAL MEDIATED LYSINE FUNCTIONALIZED AG-ZNO NANOPARTICLES FOR DYE DEGRADATION

Neelam Farheen[1], Kashif-ur-Rehman[1], Muhammad Naveed[2]

[1]Department of Biochemistry, Minhaj University Lahore-Pakistan
[2]Faculty of Science and Technology, University of Central Punjab, Lahore-Pakistan
Corresponding Author: Neelam Farheen, Email: neelamfarheen11@gmail.com

ABSTRACT

Background: Synthetic dyes released from industrial activities represent major environmental pollutants due to their persistence, toxicity, and resistance to conventional treatment methods. Nanotechnology-based remediation using green synthesized nanoparticles offers an effective and sustainable alternative for wastewater treatment and biomedical applications.
Methods: In this study, Ag–Zn bimetallic nanoparticles (Ag–Zn NPs) were synthesized using bacterial metabolites through a green synthesis approach and subsequently functionalized with lysine (Lys–Ag–Zn NPs). Structural and compositional characterization was performed using SEM, FTIR, and EDX analyses. The catalytic performance of the nanoparticles was evaluated through degradation of methylene blue and methyl orange dyes. Biological activities were assessed using antioxidant (DPPH scavenging), anti-inflammatory (protein denaturation inhibition), and anti-hemolytic assays.
Results: SEM analysis revealed nanosized particles with average sizes of approximately 74 nm for Ag–Zn NPs and 82 nm for Lys–Ag–Zn NPs. FTIR and EDX analyses confirmed successful lysine functionalization and the presence of Ag and Zn within the bimetallic structure. Dye degradation studies demonstrated concentration-dependent catalytic activity, with Lys–Ag–Zn NPs achieving up to 95% degradation compared with 92% for non-functionalized nanoparticles at 50 µg/mL. In biological assays, lysine-functionalized nanoparticles exhibited superior performance, showing 82.3% anti-inflammatory activity, 88.2% antioxidant activity, and 93.4% anti-hemolytic activity at the highest tested concentrations. These values were consistently higher than those obtained for non-functionalized nanoparticles.
Conclusion: The findings demonstrate that lysine functionalization significantly enhances the catalytic and biological performance of bacterially synthesized Ag–Zn bimetallic nanoparticles. The developed nanomaterials exhibit considerable potential for environmental remediation and biomedical applications.

Keywords: Ag–ZnO bimetallic nanoparticles, Artificial Neural Network (ANN), Green synthesis, Bacterial metabolites, Lysine functionalization, Photocatalytic dye degradation.

INTRODUCTION

Nanotechnology has emerged as one of the most promising fields for addressing environmental and biomedical challenges through the development of functional nanomaterials with enhanced physicochemical properties [1]. Among various nanomaterials, metallic and bimetallic nanoparticles have gained considerable attention due to their unique optical, catalytic, antimicrobial, antioxidant, and biocompatible characteristics. Bimetallic nanoparticles, in particular, often exhibit superior performance compared with their monometallic counterparts because of synergistic interactions between the constituent metals, resulting in improved catalytic activity, stability, and surface reactivity [2]. Recent advances in green nanotechnology have focused on environmentally benign synthesis approaches utilizing biological resources such as plant extracts, fungi, algae, and bacterial metabolites to reduce metal ions and stabilize the resulting nanoparticles.

Industrialization and urbanization have significantly increased the discharge of hazardous pollutants into aquatic ecosystems. Among these pollutants, synthetic dyes represent one of the most persistent and problematic contaminants due to their extensive use in textile, paper, leather, cosmetic, pharmaceutical, and food industries. It is estimated that a substantial fraction of industrial dyes is released into wastewater during manufacturing and processing operations [3]. Methylene blue and methyl orange are among the most commonly used dyes and are frequently detected in industrial effluents [4]. Their presence in aquatic environments reduces light penetration, disrupts photosynthetic activity, decreases dissolved oxygen levels, and negatively affects aquatic organisms. Furthermore, prolonged exposure to these dyes may cause toxic, mutagenic, and carcinogenic effects in living systems. Conventional wastewater treatment technologies, including adsorption, coagulation, flocculation, and biological treatment, often suffer from limitations such as incomplete degradation, high operational costs, and secondary pollution generation [5].

Nanoparticle-based catalytic degradation has emerged as an efficient alternative for dye remediation owing to the high surface area, tunable surface chemistry, and enhanced catalytic efficiency of nanomaterials. Silver and zinc-based nanoparticles have attracted particular interest because silver possesses strong catalytic and antimicrobial properties, while zinc contributes excellent electron-transfer characteristics and environmental compatibility [6]. The combination of silver and zinc in a bimetallic system creates synergistic effects that enhance catalytic degradation of organic pollutants and improve biological performance.

Green synthesis using bacterial metabolites offers an environmentally friendly route for nanoparticle production. Bacterial metabolites contain a variety of biomolecules, including proteins, enzymes, amino acids, polysaccharides, and reducing agents capable of mediating nanoparticle synthesis and stabilization. This approach minimizes the use of hazardous chemicals and promotes sustainable nanomaterial production. Moreover, biomolecule-mediated synthesis often produces nanoparticles with enhanced surface functionality and biological activity [7].

Surface functionalization represents an effective strategy for further improving nanoparticle performance. Lysine, an essential amino acid containing both amino and carboxyl functional groups, has been widely investigated as a biocompatible surface modifier. Functionalization with lysine enhances nanoparticle stability, prevents excessive aggregation, increases dispersibility in aqueous media, and introduces reactive functional groups that facilitate interactions with pollutants and biological targets [8]. The amino groups of lysine can promote adsorption of dye molecules onto the nanoparticle surface, thereby increasing degradation efficiency. Additionally, lysine coating may improve biocompatibility and reduce potential cytotoxic effects while enhancing antioxidant, anti-inflammatory, and hemocompatible properties.

In addition to environmental remediation, nanoparticles have demonstrated considerable biological potential. Reactive oxygen species generated during oxidative stress are associated with inflammation, cellular damage, and various chronic diseases [9]. Nanomaterials possessing antioxidant and anti-inflammatory activities may therefore contribute to biomedical applications including drug delivery, wound healing, and therapeutic interventions. Furthermore, evaluation of anti-hemolytic activity is essential for assessing the compatibility of nanoparticles with biological systems and determining their suitability for medical applications.

Therefore, the present study aimed to synthesize Ag–Zn bimetallic nanoparticles using bacterial metabolites through a green synthesis approach and subsequently functionalize them with lysine. The synthesized nanomaterials were characterized using SEM, FTIR, and EDX analyses. Their catalytic potential was investigated through degradation of methylene blue and methyl orange dyes, while their biological activities were evaluated through antioxidant, anti-inflammatory, and anti-hemolytic assays. The study provides insights into the role of lysine functionalization in enhancing both environmental and biomedical applications of bacterially synthesized Ag–Zn bimetallic nanoparticles.

2. MATERIALS AND METHODS

2.1. Artificial Neural Network (ANN) Modeling and Optimization

2.1.1. Dataset Compilation and Preprocessing

To predict and optimize the size of the synthesized zinc-silver (ZnO-Ag) bimetallic nanoparticles, a machine learning framework based on a multilayer perceptron (MLP) feed-forward Artificial Neural Network (ANN) was developed. Due to the scarcity of published data on lysine-functionalized bimetallic systems, the model was initially trained on non-functionalized bimetallic nanoparticle synthesis parameters and subsequently utilized as a predictive baseline for the lysine-conjugated synthesis [10].

The modeling dataset was constructed by extracting 200 data points from peer-reviewed literature detailing bimetallic nanoparticle synthesis under diverse environmental and chemical conditions. To enhance the model's robustness and contextual accuracy, this external dataset was supplemented with custom empirical measurements from our own

laboratory experiments. The consolidated dataset tracking the critical input variables namely reactant concentration, reaction temperature, pH, and stirring speed (RPM) alongside the target output variable (particle size) is summarized in Table 1. Prior to network training, the raw dataset was preprocessed and transformed into binary formats suitable for algorithmic ingestion (Table 2), and then partitioned into distinct subsets for training, validation, and testing.

2.1.2. Network Architecture and Algorithmic Training

The topology of the MLP network consisted of an input layer accommodating the experimental parameters (concentration, temperature, pH, and RPM) and a single output layer representing the predicted nanoparticle size. Network training was executed using the Levenberg-Marquardt (LM) backpropagation algorithm, selected for its rapid convergence and computational efficiency in non-linear optimization tasks.

To introduce non-linearity into the network hidden layer, a hyperbolic tangent sigmoid activation function was employed, while a pure linear activation function was applied at the output layer to yield continuous size predictions. The predictive accuracy, robustness, and generalization capability of the trained ANN model were rigorously evaluated using two statistical metrics: the coefficient of determination (R^2) and the Mean Absolute Percentage Error (MAPE).

The optimal experimental conditions determined by the ANN framework were successfully applied as a benchmark reference to guide and streamline the green synthesis of both the core bimetallic nanoparticles and their subsequent lysine-conjugated derivatives, significantly minimizing manual experimental trials [11].

Table 1. Experimental dataset parameters for Artificial Neural Network (ANN) model for Ag–Zn bimetallic nanoparticles.

Nanoparticle_ID	pH	Concentration_M	RPM	Temperature_C	Size_nm
Ag-ZnNP	7.56	0.0352	1014	57	83.88
Ag-ZnNP	10.73	0.0273	211	67	115.75
Ag-ZnNP	9.53	0.0162	517	79	96.82
Ag-ZnNP	8.79	0.0409	791	82	116.72
Ag-ZnNP	6.36	0.0346	415	21	78.24
Ag-ZnNP	6.36	0.009	538	30	48.78
Ag-ZnNP	5.82	0.0456	975	83	96.95
Ag-ZnNP	10.26	0.0413	1190	40	81.78
Ag-ZnNP	8.81	0.0475	860	37	96.72
Ag-ZnNP	9.39	0.0366	280	83	120
Ag-ZnNP	5.61	0.0311	926	57	69.09
Ag-ZnNP	10.83	0.0215	684	51	93.11
Ag-ZnNP	10.08	0.0467	573	30	98.43
Ag-ZnNP	6.67	0.0434	1175	64	82.84
Ag-ZnNP	6.5	0.0032	909	52	47.64
Ag-ZnNP	6.51	0.0023	399	60	66.06
Ag-ZnNP	7.17	0.0194	736	27	61.56
Ag-ZnNP	8.39	0.0407	665	30	90.67
Ag-ZnNP	7.88	0.0494	288	70	120
Ag-ZnNP	7.1	0.0084	467	60	75.41
Ag-ZnNP	8.87	0.0301	854	36	75.01
Ag-ZnNP	6.27	0.0197	770	65	72.73
Ag-ZnNP	7.11	0.0485	1121	51	86.39
Ag-ZnNP	7.51	0.0423	688	73	104.5
Ag-ZnNP	8.01	0.0421	1076	39	79.54
Ag-ZnNP	9.82	0.024	737	52	89.68

Ag-ZnNP	6.6	0.0213	246	59	86.9
Ag-ZnNP	8.33	0.0144	487	51	82.56
Ag-ZnNP	8.76	0.0038	977	21	37.26
Ag-ZnNP	5.76	0.0434	215	52	104.68
Ag-ZnNP	8.84	0.0408	910	49	86.87
Ag-ZnNP	6.44	0.05	600	52	107.47
Ag-ZnNP	5.86	0.0498	1118	45	77.05
Ag-ZnNP	10.72	0.0282	993	41	78.04
Ag-ZnNP	10.81	0.0387	1180	85	109.19
Ag-ZnNP	9.95	0.0473	285	57	120
Ag-ZnNP	7.18	0.0426	449	65	109.04
Ag-ZnNP	6.04	0.0131	590	34	60.3
Ag-ZnNP	9.26	0.0231	981	63	80.57
Ag-ZnNP	7.92	0.0073	534	68	80.48
Ag-ZnNP	6.17	0.0477	828	80	101.31
Ag-ZnNP	8.22	0.0307	718	86	108.66
Ag-ZnNP	5.69	0.0122	336	25	57.62
Ag-ZnNP	10.5	0.0339	1082	28	77.28
Ag-ZnNP	6.92	0.0313	887	25	62.92
Ag-ZnNP	9.14	0.0185	1039	51	68.63
Ag-ZnNP	7.21	0.0066	697	60	68.47
Ag-ZnNP	8.36	0.0339	1026	27	64.34
Ag-ZnNP	8.51	0.0265	926	69	83.54
Ag-ZnNP	6.52	0.0388	676	81	103.85
Ag-ZnNP	10.83	0.0265	793	81	108.65
Ag-ZnNP	9.76	0.0428	422	26	99.77
Ag-ZnNP	10.67	0.028	1189	23	65.9
Ag-ZnNP	10.42	0.0285	571	25	84.97
Ag-ZnNP	8.79	0.044	1134	77	104.69
Ag-ZnNP	10.57	0.0208	1194	41	67.34
Ag-ZnNP	5.99	0.0076	601	45	58.28
Ag-ZnNP	6.58	0.0024	642	22	41.46
Ag-ZnNP	5.75	0.038	689	60	89.66
Ag-ZnNP	7.29	0.0314	814	79	96.06
Ag-ZnNP	7.64	0.0355	472	33	86.87
Ag-ZnNP	6.99	0.0114	725	31	53.32
Ag-ZnNP	10.06	0.0077	358	31	74.39
Ag-ZnNP	7.46	0.0017	351	32	55.58
Ag-ZnNP	7.05	0.0182	1194	44	51.25
Ag-ZnNP	8.48	0.0299	819	64	94.78
Ag-ZnNP	6.28	0.0202	387	38	69.16
Ag-ZnNP	9.91	0.0224	1012	74	85.11
Ag-ZnNP	5.91	0.0453	297	64	108.87

Ag-ZnNP	10.93	0.0181	330	27	82.86
Ag-ZnNP	9.75	0.0262	1004	72	94.87
Ag-ZnNP	6.59	0.0394	370	74	108.84
Ag-ZnNP	5.53	0.0204	1135	51	51.12
Ag-ZnNP	9.99	0.0315	1185	70	90.45
Ag-ZnNP	9.39	0.0433	382	63	120
Ag-ZnNP	9.51	0.0475	1182	89	115.1
Ag-ZnNP	9.74	0.0082	563	37	63.66
Ag-ZnNP	5.91	0.0464	238	41	99.03
Ag-ZnNP	7.47	0.0251	726	56	81.83
Ag-ZnNP	6.14	0.0137	1087	75	63.16
Ag-ZnNP	10.25	0.0235	696	78	103.85
Ag-ZnNP	8.93	0.049	715	22	93.57
Ag-ZnNP	7.32	0.0251	548	47	83.95
Ag-ZnNP	5.85	0.0171	1181	54	45.36
Ag-ZnNP	7.21	0.032	1120	80	84.1
Ag-ZnNP	7.29	0.0128	596	73	81.75
Ag-ZnNP	9.51	0.0047	921	82	82.66
Ag-ZnNP	9.01	0.0073	360	26	65.11
Ag-ZnNP	10.38	0.0073	215	68	96.1
Ag-ZnNP	8.1	0.0084	692	50	68.47
Ag-ZnNP	6.16	0.0078	625	77	73.13
Ag-ZnNP	9.42	0.0324	307	80	120
Ag-ZnNP	9.68	0.0099	1093	43	57.79
Ag-ZnNP	8.59	0.0179	649	39	73.96
Ag-ZnNP	9.74	0.0449	510	56	114.17
Ag-ZnNP	8.22	0.0242	938	23	60.84
Ag-ZnNP	8.38	0.0337	369	39	93.03
Ag-ZnNP	7.85	0.0094	745	79	77.9
Ag-ZnNP	5.64	0.0104	613	43	56.67
Ag-ZnNP	6.09	0.003	450	69	67.04
Ag-ZnNP	5.67	0.0093	958	68	58.07
Ag-ZnNP	9	0.0147	980	70	80.33
Ag-ZnNP	7.23	0.0097	340	55	73.37
Ag-ZnNP	8.3	0.0053	473	85	90.71
Ag-ZnNP	10.49	0.0069	615	53	77.36
Ag-ZnNP	6.87	0.0236	807	55	74.82
Ag-ZnNP	7.76	0.0111	938	25	48.79
Ag-ZnNP	9.66	0.0188	1090	58	69.05
Ag-ZnNP	6.76	0.0257	238	61	91.07
Ag-ZnNP	5.92	0.0348	1013	77	83.85
Ag-ZnNP	7.09	0.0029	228	31	60.01
Ag-ZnNP	6.39	0.0402	1157	22	57.94

Ag-ZnNP	10.61	0.0318	676	37	91.25
Ag-ZnNP	9.94	0.005	517	59	86.53
Ag-ZnNP	8.98	0.0438	444	40	100.44
Ag-ZnNP	10.29	0.0461	947	34	95.65
Ag-ZnNP	9.92	0.004	896	45	60.49
Ag-ZnNP	6.53	0.0146	471	27	61.1
Ag-ZnNP	10.41	0.0405	639	61	118.58
Ag-ZnNP	8.47	0.0377	947	63	95.54
Ag-ZnNP	9.94	0.01	438	33	74.08
Ag-ZnNP	10.43	0.0113	576	21	69.76
Ag-ZnNP	7.25	0.0192	465	56	84.98
Ag-ZnNP	6.11	0.0247	1125	88	76.27
Ag-ZnNP	6.75	0.0313	1120	57	72.05
Ag-ZnNP	7.85	0.0191	558	60	80.1
Ag-ZnNP	10	0.0237	539	81	109.12
Ag-ZnNP	10.23	0.0376	588	79	120
Ag-ZnNP	5.54	0.0028	776	33	38.22
Ag-ZnNP	8.31	0.0134	1189	21	40.55
Ag-ZnNP	7.8	0.036	888	89	105.17
Ag-ZnNP	6.72	0.0449	202	36	100.06
Ag-ZnNP	6.16	0.0261	628	47	73.61
Ag-ZnNP	7.36	0.0271	341	85	105.82
Ag-ZnNP	10.69	0.0063	575	54	85.12
Ag-ZnNP	7.28	0.0229	869	24	55.87
Ag-ZnNP	8.35	0.0271	523	84	109.46
Ag-ZnNP	9.37	0.0129	345	59	93.9
Ag-ZnNP	7.5	0.0142	1157	75	67.84
Ag-ZnNP	10.84	0.0195	492	55	94.6
Ag-ZnNP	10.79	0.002	864	64	74.83
Ag-ZnNP	6.88	0.0168	631	42	69.17
Ag-ZnNP	8.23	0.0114	904	66	72.64
Ag-ZnNP	7.15	0.017	1148	50	52.47
Ag-ZnNP	7.07	0.0069	1174	30	36.07
Ag-ZnNP	5.7	0.0446	784	29	77.64
Ag-ZnNP	8.85	0.0301	598	86	111.09
Ag-ZnNP	8.26	0.0343	1016	33	72.71
Ag-ZnNP	5.78	0.0397	1088	29	62.21
Ag-ZnNP	7.03	0.0254	543	20	65.35
Ag-ZnNP	10.5	0.0053	1163	24	40.39
Ag-ZnNP	6.82	0.0273	339	39	84.48
Ag-ZnNP	6.3	0.0298	386	27	76.52
Ag-ZnNP	8.19	0.0375	1004	62	91.4
Ag-ZnNP	10.92	0.0222	260	20	88.52

Ag-ZnNP	6.83	0.0073	1196	76	59.57
Ag-ZnNP	9.2	0.0149	1138	83	82.8
Ag-ZnNP	9.69	0.0188	579	47	78.77
Ag-ZnNP	6.81	0.0326	909	56	82.44
Ag-ZnNP	9.51	0.029	1006	66	90.52
Ag-ZnNP	7.52	0.0184	639	56	78.73
Ag-ZnNP	8.98	0.0493	518	68	120
Ag-ZnNP	8.98	0.0307	501	63	104.91
Ag-ZnNP	8.45	0.0126	543	75	92.59
Ag-ZnNP	6	0.006	210	47	67.82
Ag-ZnNP	10.09	0.0085	261	25	73.19
Ag-ZnNP	7.26	0.0131	1044	80	72.58
Ag-ZnNP	6.53	0.0089	425	39	53.59
Ag-ZnNP	5.72	0.0101	352	21	51.69
Ag-ZnNP	8.75	0.015	910	56	69.64
Ag-ZnNP	9.23	0.0095	763	39	67.27
Ag-ZnNP	5.59	0.0449	971	45	79.18
Ag-ZnNP	8.32	0.0049	770	48	59.93
Ag-ZnNP	6.75	0.0267	783	20	58.19
Ag-ZnNP	9.05	0.0211	859	54	78.33
Ag-ZnNP	6.46	0.0491	1060	89	103.71
Ag-ZnNP	9.3	0.0065	774	78	79.7
Ag-ZnNP	7.63	0.0205	509	88	96.8
Ag-ZnNP	10.65	0.0485	1084	52	102.23
Ag-ZnNP	6.26	0.0434	442	70	110.11
Ag-ZnNP	7.38	0.041	692	31	81.55
Ag-ZnNP	6.12	0.0136	565	39	61.66
Ag-ZnNP	10.59	0.0094	529	72	97.28
Ag-ZnNP	10.33	0.0338	306	62	113.48
Ag-ZnNP	6.92	0.0465	425	69	113.07
Ag-ZnNP	9.13	0.0283	1024	48	75.67
Ag-ZnNP	9.99	0.029	417	76	119.49
Ag-ZnNP	8.55	0.0147	1136	58	68.09
Ag-ZnNP	8.41	0.0387	952	75	98.36
Ag-ZnNP	6.83	0.0102	705	62	69.78
Ag-ZnNP	6.01	0.0169	458	69	84.19
Ag-ZnNP	10.43	0.0218	1087	42	73.44
Ag-ZnNP	10.45	0.0259	973	63	91.34
Ag-ZnNP	8.98	0.0129	716	57	80.94
Ag-ZnNP	7.36	0.0066	972	42	46.66
Ag-ZnNP	7.42	0.0309	253	64	101.96
Ag-ZnNP	9.49	0.0151	246	71	99.63
Ag-ZnNP	10.43	0.0295	926	69	101.26

Ag-ZnNP	10.38	0.0086	888	27	55.86
Ag-ZnNP	9.79	0.0246	720	20	70.21

Table 2. Preprocessed and transformed binary dataset representing the experimental input conditions

Ag-ZnNP	pH	Concentration	RPM	Temperature	Size_nm
1	0	1	1	1	1
1	1	1	0	1	1
1	1	0	0	1	1
1	1	1	1	1	1
1	0	1	0	0	0
1	0	0	0	0	0
1	0	1	1	1	1
1	1	1	1	0	1
1	1	1	1	0	1
1	1	1	0	1	1
1	0	1	1	1	0
1	1	0	0	0	1
1	1	1	0	0	1
1	0	1	1	1	1
1	0	0	1	0	0
1	0	0	0	1	0
1	0	0	1	0	0
1	1	1	0	0	1
1	0	1	0	1	1
1	0	0	0	1	0
1	1	1	1	0	0
1	0	0	1	1	0
1	0	1	1	0	1
1	0	1	0	1	1
1	0	1	1	0	0
1	1	1	1	0	1
1	0	0	0	1	1
1	1	0	0	0	1
1	1	0	1	0	0
1	0	1	0	0	1
1	1	1	1	0	1
1	0	1	0	0	1
1	0	1	1	0	0
1	1	1	1	0	0
1	1	1	1	1	1
1	1	1	0	1	1
1	0	1	0	1	1
1	0	0	0	0	0

1	1	0	1	1	0
1	0	0	0	1	0
1	0	1	1	1	1
1	1	1	1	1	1
1	0	0	0	0	0
1	1	1	1	0	0
1	0	1	1	0	0
1	1	0	1	0	0
1	0	0	0	1	0
1	1	1	1	0	0
1	1	1	1	1	1
1	0	1	0	1	1
1	1	1	1	1	1
1	1	1	0	0	1
1	1	1	1	0	0
1	1	1	0	0	1
1	1	1	1	1	1
1	1	0	1	0	0
1	0	0	0	0	0
1	0	0	0	0	0
1	0	1	0	1	1
1	0	1	1	1	1
1	0	1	0	0	1
1	0	0	1	0	0
1	1	0	0	0	0
1	0	0	0	0	0
1	0	0	1	0	0
1	1	1	1	1	1
1	0	0	0	0	0
1	1	0	1	1	1
1	0	1	0	1	1
1	1	0	0	0	1
1	1	1	1	1	1
1	0	1	0	1	1
1	0	0	1	0	0
1	1	1	1	1	1
1	1	1	0	1	1
1	1	1	1	1	1
1	1	0	0	0	0
1	0	1	0	0	1
1	0	1	1	1	1
1	0	0	1	1	0
1	1	0	0	1	1

1	1	1	1	0	1
1	0	1	0	0	1
1	0	0	1	0	0
1	0	1	1	1	1
1	0	0	0	1	1
1	1	0	1	1	1
1	1	0	0	0	0
1	1	0	0	1	1
1	0	0	0	0	0
1	0	0	0	1	0
1	1	1	0	1	1
1	1	0	1	0	0
1	1	0	0	0	0
1	1	1	0	1	1
1	1	1	1	0	0
1	1	1	0	0	1
1	0	0	1	1	0
1	0	0	0	0	0
1	0	0	0	1	0
1	0	0	1	1	0
1	1	0	1	1	0
1	0	0	0	1	0
1	1	0	0	1	1
1	1	0	0	0	0
1	0	0	1	1	0
1	0	0	1	0	0
1	1	0	1	1	0
1	0	1	0	1	1
1	0	1	1	1	1
1	0	0	0	0	0
1	0	1	1	0	0
1	1	1	0	0	1
1	1	0	0	1	1
1	1	1	0	0	1
1	1	1	1	0	1
1	1	0	1	0	0
1	0	0	0	0	0
1	1	1	0	1	1
1	1	1	1	1	1
1	1	0	0	0	0
1	1	0	0	0	0
1	0	0	0	1	1
1	0	1	1	1	0

1	0	1	1	1	0
1	0	0	0	1	0
1	1	0	0	1	1
1	1	1	0	1	1
1	0	0	1	0	0
1	1	0	1	0	0
1	0	1	1	1	1
1	0	1	0	0	1
1	0	1	0	0	0
1	0	1	0	1	1
1	1	0	0	0	1
1	0	0	1	0	0
1	1	1	0	1	1
1	1	0	0	1	1
1	0	0	1	1	0
1	1	0	0	1	1
1	1	0	1	1	0
1	0	0	0	0	0
1	1	0	1	1	0
1	0	0	1	0	0
1	0	0	1	0	0
1	0	1	1	0	0
1	1	1	0	1	1
1	1	1	1	0	0
1	0	1	1	0	0
1	0	1	0	0	0
1	1	0	1	0	0
1	0	1	0	0	1
1	0	1	0	0	0
1	0	1	1	1	1
1	1	0	0	0	1
1	0	0	1	1	0
1	1	0	1	1	1
1	1	0	0	0	0
1	0	1	1	1	1
1	1	1	1	1	1
1	0	0	0	1	0
1	1	1	0	1	1
1	1	1	0	1	1
1	1	0	0	1	1
1	0	0	0	0	0
1	1	0	0	0	0
1	0	0	1	1	0

1	0	0	0	0	0
1	0	0	0	0	0
1	1	0	1	1	0
1	1	0	1	0	0
1	0	1	1	0	0
1	1	0	1	0	0
1	0	1	1	0	0
1	1	0	1	0	0
1	0	1	1	1	1
1	1	0	1	1	0
1	0	0	0	1	1
1	1	1	1	0	1
1	0	1	0	1	1
1	0	1	0	0	1
1	0	0	0	0	0
1	1	0	0	1	1
1	1	1	0	1	1
1	0	1	0	1	1
1	1	1	1	0	0
1	1	1	0	1	1
1	1	0	1	1	0
1	1	1	1	1	1
1	0	0	1	1	0
1	0	0	0	1	1
1	1	0	1	0	0
1	1	1	1	1	1
1	1	0	1	1	0
1	0	0	1	0	0
1	0	1	0	1	1
1	1	0	0	1	1
1	1	1	1	1	1
1	1	0	1	0	0
1	1	1	1	0	0

2.2. Synthesis and Functionalization of Lysine-Conjugated Ag-ZnO Nanoparticles

2.2.1. Microbial Culture, Fermentation, and Extraction of Metabolites

To obtain an adequate biomass for the bioreduction process, a 500 mL inoculum of Georgenia satyanarayanai strain MBBL (GenBank accession no. PV892497.1) was prepared. Concurrently, a 500 mL formulation of production medium consisting of oatmeal, corn, tryptone, sodium chloride (NaCl), and phenol red dissolved in distilled water was homogenized. The bacterial inoculum was subsequently introduced into the prepared fermentation medium. The culture was maintained in a shaking incubator under continuous agitation and aeration to ensure uniform nutrient distribution and optimal aerobic growth [12].

Following a 14-day incubation period, the fermentation broth was subjected to centrifugation at 4000rpm for 30 min at 4°C to pellet the bacterial cells. The cell-free supernatant, containing the secreted extracellular metabolites, was harvested and stored for use as the reducing and stabilizing agent during nanoparticle synthesis [13].

2.2.2. Preparation of Precursor and Functionalization Solutions

Aqueous stock solutions (1M) of the silver (Ag) and zinc oxide (ZnO) precursors were prepared independently by dissolving silver nitrate ($AgNO_3$) and zinc oxide in distilled water. To prevent photo-induced reduction, the preparation was conducted under dark conditions, and the storage vessels were wrapped in aluminum foil. Working solutions (0.25M) were subsequently prepared via volumetric dilution of the stock solutions immediately prior to use. Additionally, a 1M aqueous solution of L-lysine was prepared in distilled water to serve as the functionalizing ligand [10].

2.2.3. Biosynthesis of Ag-ZnO Bimetallic Nanoparticles

For the synthesis of the bimetallic Ag–ZnO nanoparticles, the 0.25M silver nitrate solution, 0.25M zinc oxide solution, and the cell-free bacterial supernatant were combined in a strict 1:1:9 (v/v/v) ratio. The precursor solutions were introduced dropwise into the metabolite supernatant under vigorous magnetic stirring at 1500\rpm in the absence of light. Upon completion of the reaction, the colloidal suspension was centrifuged at 4000rpm for 30 min to isolate the synthesized nanomaterial. The resulting pellet was washed three times with distilled water to eliminate unreacted precursors and residual media components, yielding purified bimetallic nanoparticles 10].

2.3. Characterization of Nanoparticles

The optical properties, surface morphology, and surface functional groups of the biosynthesized Ag-ZnO and functionalized Lys–Ag-ZnO nanoparticles (NPs) were comprehensive evaluated using multiple analytical techniques.

2.3.1. UV–Visible Spectrophotometry

UV–Vis spectrophotometry was employed to confirm the successful formation and evaluate the optical characteristics of both the Ag–ZnO and Lys–Ag–ZnO NPs. The absorbance profiles of the colloidal suspensions were recorded across a spectral scanning range of 200–800 nm, using distilled water as the baseline blank. Synthesis confirmation was monitored via the appearance of characteristic absorption bands corresponding to intrinsic band-gap transitions and specific surface plasmon resonance (SPR) peaks [14].

2.3.2. Scanning Electron Microscopy (SEM)

The surface topography, spatial geometry, and structural morphology of the Ag–ZnO and Lys–Ag–ZnO NPs were examined via scanning electron microscopy (SEM). For sample preparation, a minute volume of the respective nanoparticle suspensions was drop-cast onto clean glass substrates or aluminum stubs and desiccated at ambient room temperature. The completely dried specimens were subsequently secured onto stubs using conductive carbon adhesive tape and sputter-coated with a thin film of platinum-gold to improve surface conductivity and minimize charging artifacts during analysis. SEM micrographs were captured at an accelerating voltage of 12.5 kV to ascertain particle size distribution, structural morphology, and surface features [15].

2.3.3. Fourier Transform Infrared (FTIR) Spectroscopy

Fourier Transform Infrared (FTIR) spectroscopy was carried out to identify the surface functional groups and confirm the surface modification/conjugation of the nanoparticles with lysine. To prepare the analytical samples, the nanoparticle suspensions were first isolated via high-speed centrifugation at 10,000 rpm for 30 min. The resulting pellet was subjected to multiple sequential washing cycles with distilled water to eliminate residual unreacted compounds, followed by drying at room temperature to yield a fine powder. The dried nanomaterial was then thoroughly blended with potassium bromide (KBr) and compressed under hydraulic pressure to form translucent pellets. FTIR spectra were acquired over a scanning range of 4000 – 400 cm^{-1} at a resolution of 4 cm-1 [16].

2.4 Dyes Degradation Analysis

The dye degradation efficiency of Ag–ZnO nanoparticles (Ag–ZnO NPs) and lysine-functionalized Ag–ZnO nanoparticles (Lys–Ag–ZnO NPs) was investigated by exposing dye-containing solutions to the synthesized nanoparticles under controlled experimental conditions. A predetermined concentration of dye solution was prepared and mixed with the nanoparticles at a dye-to-nanoparticle ratio of 1:1. The resulting mixtures were continuously agitated to facilitate effective interaction between the dye molecules and nanoparticles. All experiments were performed under standardized environmental conditions for a fixed incubation period. At selected time intervals, aliquots were withdrawn and analyzed using UV–Visible spectroscopy to determine the remaining dye concentration [13, 17]. The degradation efficiency was estimated from the absorbance measurements, where A_0 represents the initial absorbance and A_t represents the absorbance at a specific time (t), according to the following equation:

$$\eta\ \% = (A_0 - A_t) / A_0 \times 100\%$$

2.5 Biological Potential of Ag–ZnO NPs and Lys–Ag–ZnO NPs

The biological activities of Ag–ZnO NPs and Lys–Ag–ZnO NPs were assessed through anti-inflammatory, antioxidant, and anti-hemolytic assays. All experiments were carried out in triplicate to ensure reproducibility and reliability of the results.

2.5.1 Anti-inflammatory Analysis

The anti-inflammatory activity was determined using the protein denaturation inhibition assay. Briefly, 2.8 mL of phosphate buffer was combined with 0.2 mL of freshly prepared egg albumin. Nanoparticle suspensions at concentrations of 100, 200, 300, 400, and 500 µg/mL were added to the reaction mixtures. The samples were incubated at 37°C for 20 minutes and subsequently heated in a water bath at 70°C for 5 minutes. After cooling to ambient temperature, absorbance readings were recorded at 660 nm using a spectrophotometer. Aspirin prepared at identical concentrations served as the reference standard [18]. The percentage inhibition of protein denaturation was calculated using the following formula:

$$\% \text{ inhibition} = (1 - At / Ac) \times 100$$

Where At is the absorbance of the test sample and Ac is the absorbance of the control.

2.5.2 Anti-oxidant Analysis

The antioxidant potential of the nanoparticles was evaluated by the DPPH (2,2-diphenyl-1-picrylhydrazyl) free radical scavenging assay. A 0.1 mM DPPH solution was prepared by dissolving 3.94 mg of DPPH in 100 mL of methanol. The solution was prepared under dark conditions and stored in a light-protected container wrapped with aluminum foil. Nanoparticle samples were prepared at concentrations of 200, 400, 600, 800, and 1000 µg/mL. For each assay, 0.1 mL of DPPH solution was mixed with the respective nanoparticle sample and incubated in the dark at room temperature for 30 minutes. Following incubation, absorbance was measured at 517 nm using a spectrophotometer [19]. A DPPH–methanol solution without nanoparticles was used as the control.

$$\% \text{ DPPH inhibition} = (Ac - As / Ac) \times 100$$

Where Ac represents the absorbance of the control and As represents the absorbance of the sample.

2.5.3 Anti-hemolytic Analysis

The hemolytic assay was conducted to evaluate the biocompatibility of the synthesized nanoparticles using human red blood cells (RBCs). Approximately 2 mL of whole blood was collected in a lithium heparin tube and centrifuged at 850 rpm for 5 minutes. The resulting RBC pellet was washed three times with phosphate-buffered saline (PBS), and the supernatant was discarded after each washing step. The washed RBCs were then resuspended in PBS to a final volume of 20 mL to obtain a homogeneous suspension.

For the assay, 180 µL of RBC suspension was mixed with nanoparticle samples at concentrations of 100, 200, 300, 400, and 500 µg/mL. The mixtures were incubated at 80 rpm for 30 minutes. After incubation, the samples were placed on ice for 5 minutes and centrifuged at 1310 rpm. Subsequently, 100 µL of the supernatant was collected and diluted with 900 µL of PBS. Absorbance was measured at 630 nm using a spectrophotometer. Triton X-100 (10%) was used as the positive control, whereas PBS served as the negative control [20]. The percentage hemolysis was calculated using the following equation:

$$\% \text{ hemolysis} = (\text{Abs. of sample} - \text{Abs. of negative control}) / \text{The abs. of positive control} \times 100$$

3. RESULTS

3.1 Artificial Neural Network (ANN) Modeling Results

The predictive capability and architectural stability of the developed multilayer perceptron (MLP) Artificial Neural Network (ANN) for the green synthesis of zinc-silver (Ag-ZnO) bimetallic nanoparticles were comprehensively evaluated using performance, training state, regression, and error distribution analyses (Figure 1). The regression plots demonstrating the relationship between the experimental target values and the network's predicted outputs across the partitioned data subsets are presented in Figure 1A. The model displayed exceptional predictive accuracy, yielding high correlation coefficients (R) of 0.998 for training, 0.991 for validation, and 0.97156 for testing, culminating in an overall global R-value of 0.9923. Notably, within the validation dataset, the network accurately mapped non-linear synthesis trends, precisely evaluating a target bimetallic nanoparticle size of 74.39 nm with a predicted size of 71.9597 nm.

The training dynamics monitored over the optimization phase are illustrated through the network's gradient steps, Marquardt damping factor, and validation failure metrics (Figure 1B). The training session successfully terminated at

epoch 10 after triggering six consecutive validation check failures, preventing overfitting and ensuring model generalizability. At the terminal epoch, the gradient magnitude minimized smoothly to 8.2679, while the control parameter stabilized at 0.01. This convergence profile correlates directly with the Mean Squared Error tracking history (Figure 1C), where the network achieved its optimal validation performance at epoch 4 with a minimal baseline of 8.33.

To evaluate the residual variance of the optimized network, an error histogram detailing the frequency distribution of deviations across 20 numerical bins was constructed (Figure 1D). The error profile exhibits a highly symmetrical, Gaussian-like distribution centered tightly around the zero-error threshold line. The maximum instance density for the training, validation, and testing datasets was clustered at a minimal error bin value of 0.03969. This minimal residual distribution confirms that the backpropagation framework effectively minimized systematic errors during parameter optimization, establishing the ANN as a highly reliable, data-driven tool for modeling and predicting the size parameters of the biosynthesized (Ag-ZnO) bimetallic nanomaterials.

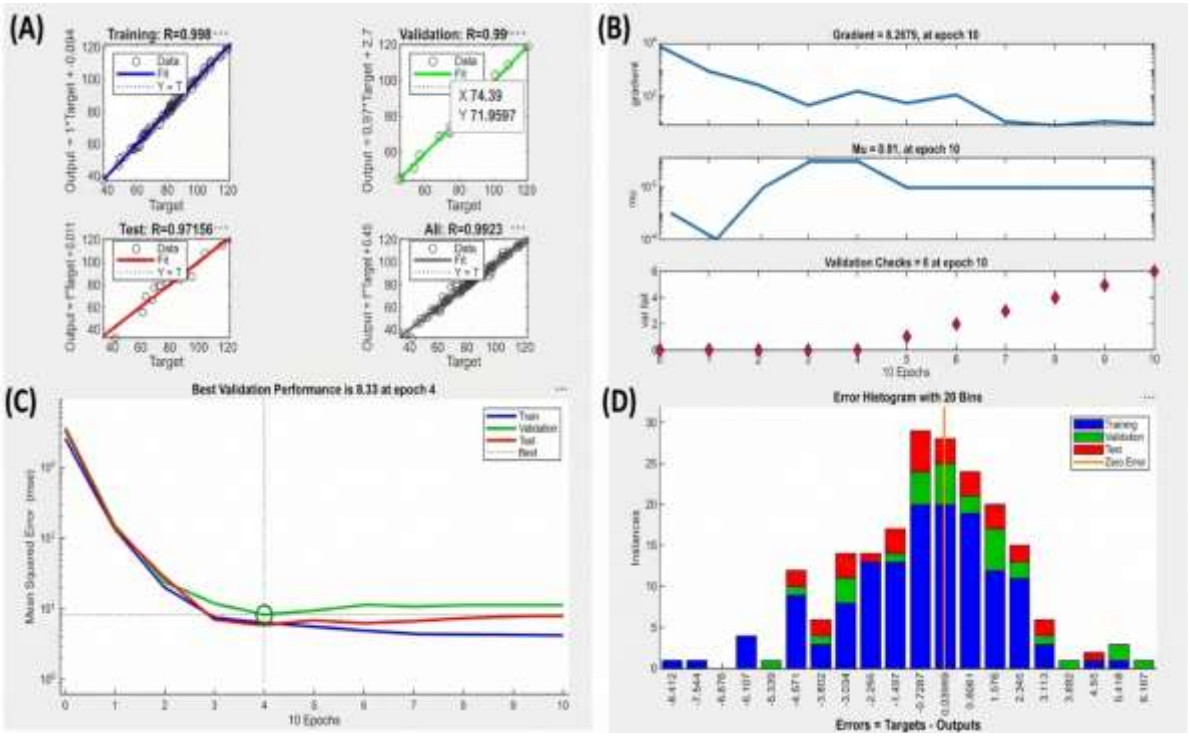

Figure 1. valuation metrics of the optimized feed-forward Artificial Neural Network (ANN) model for (Ag-ZnO) bimetallic nanoparticle size prediction: (A) Linear regression analysis comparing experimental targets and model outputs for training, validation, testing, and combined datasets; (B) Training state parameters showing gradient, damping factor, and validation failures across 10 epochs; (C) Mean squared error convergence curves identifying the best validation performance at epoch 4; and (D) Error histogram distribution using 20 distinct bins relative to the zero-error axis.

3.2. Synthesis of Lysine-Functionalized Ag-ZnO Bimetallic Nanoparticles

The biosynthesis of silver-zinc oxide (Ag-ZnO) bimetallic nanoparticles was carried out under the optimized parameter boundaries derived from the Artificial Neural Network (ANN) modeling framework. The initial phase of the bioreduction reaction was visually marked by a distinct color transition and the emergence of a stable colloidal suspension, signifying successful nucleation and subsequent nanocrystal growth.

Upon the subsequent introduction of the L-lysine ligand for surface functionalization, a slight increase in turbidity was observed alongside a pronounced enhancement in colloidal stability, indicating effective surface modification and steric stabilization preventing nanoparticle aggregation. The successful formation of the core bimetallic structure and its subsequent conjugation with the amino acid ligand were systematically validated via UV–Visible spectrophotometry, scanning electron microscopy (SEM), and Fourier transform infrared (FTIR) spectroscopy.

UV-Visible spectroscopy

The optical properties and structural evolution of the unfunctionalized Ag-ZnO bimetallic nanoparticles and their lysine-functionalized Ag-ZnO counterparts were systematically monitored via UV–Visible spectrophotometry across a 200–600 nm scanning range. The pristine Ag-ZnO spectrum exhibits a high-energy band-gap transition at 225 nm, a secondary peak at 275 nm, and a well-defined Surface Plasmon Resonance (SPR) peak centered at 405 nm; the concurrent presence of these ultraviolet and visible absorption bands confirms the successful coupled nucleation of both silver and zinc components within a single bimetallic framework. Upon surface modification with L-lysine, successful ligand conjugation was verified by clear spectral modifications: the high-energy peaks underwent bathochromic shifts to 235 nm and 278 nm, respectively, while the primary SPR band exhibited a hypsochromic shift from 405 nm to 398 nm with a corresponding decrease in absolute absorbance intensity. These systematic band deviations and plasmon stabilization directly demonstrate the altered local dielectric environment and surface electronic density induced by the chemisorption and capping of the L-lysine ligand onto the bimetallic interfaces.

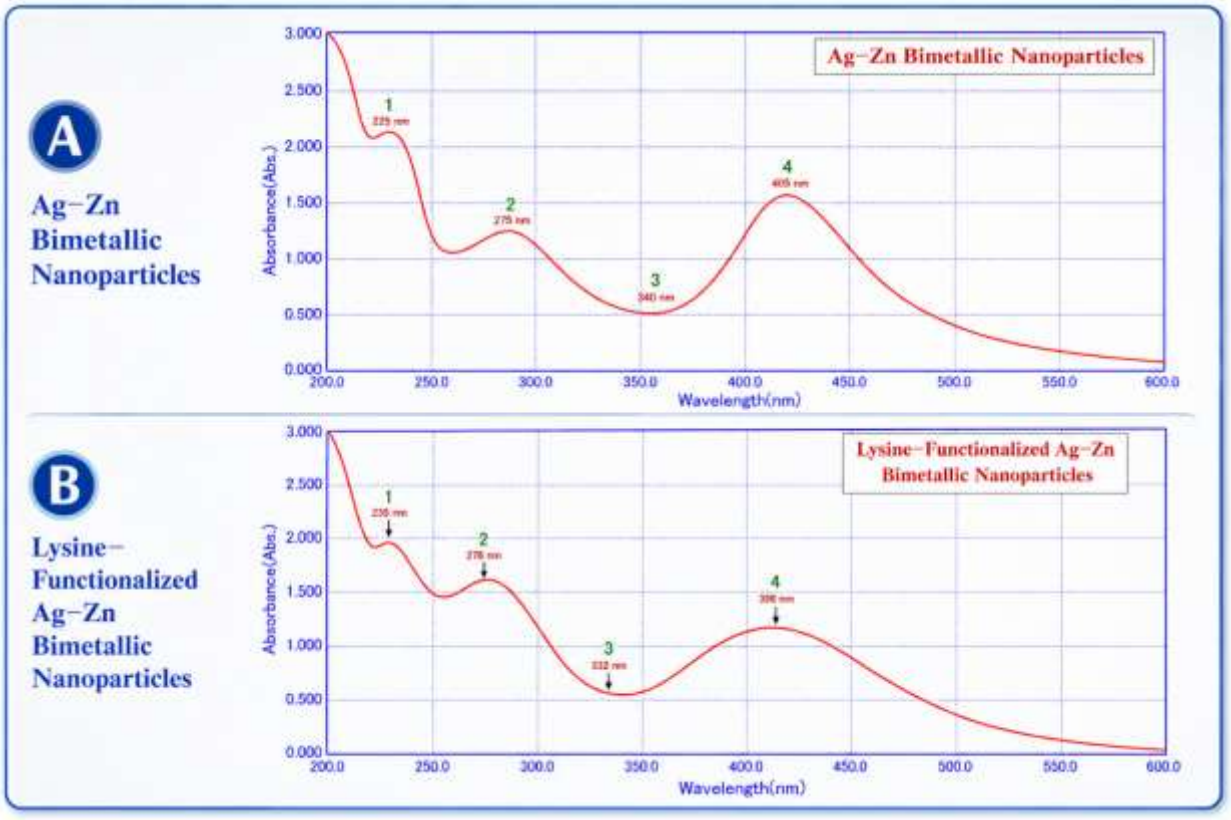

Figure 2. UV–Visible absorption spectra of synthesized nanoparticles. **(A)** Ag–Zn bimetallic nanoparticles showing characteristic absorption bands at 225, 275, 340, and 405 nm. **(B)** Lysine-functionalized Ag–Zn bimetallic nanoparticles exhibiting absorption features at 235, 278, 332, and 398 nm.

Scanning Electron Microscopy

The surface topography and size characteristics of the nanomaterials were evaluated via SEM (Figure 3). The pristine Ag-ZnO bimetallic matrix (Figure 3A) exhibits localized clusters embedded in the bio-organic template, with a representative particle diameter of 74 nm—closely matching the 71.96 nm size baseline predicted by the ANN model. Conversely, the lysine-functionalized Ag-ZnO nanoparticles (Figure 3B) demonstrate a morphological shift to a highly dense, uniform, and granular assembly of spherical structures with a distinct size increase to 82 nm. This 8 nm dimensional expansion provides direct physical evidence of successful surface modification, confirming that the L-lysine ligand successfully capped the metallic cores to form a stabilizing organic shell.

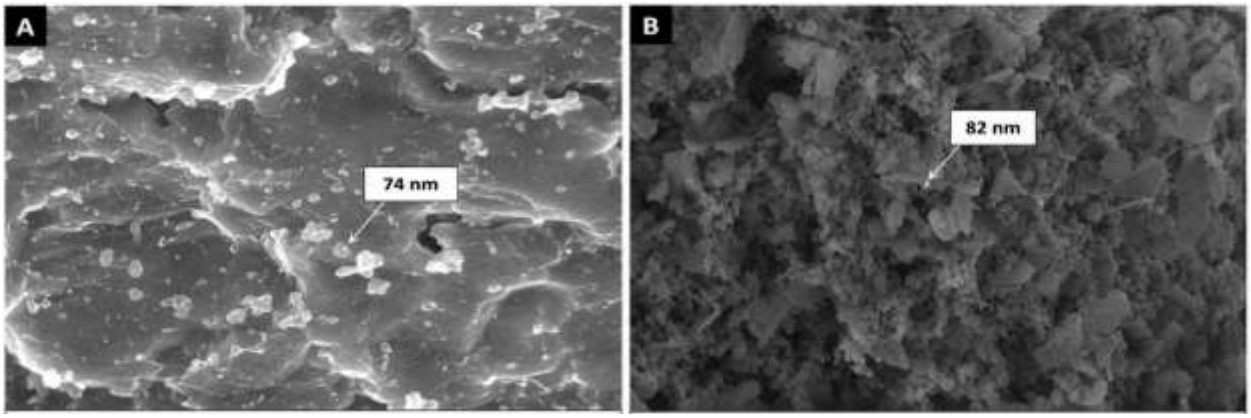

Figure 3. Scanning electron microscopy (SEM) images of Ag–Zn bimetallic nanoparticles. (A) SEM micrograph showing dispersed nanoparticles with an average particle size of approximately **74 nm**. (B) SEM micrograph showing densely agglomerated nanoparticles with an average particle size of approximately **82 nm**.

Fourier Transform Infrared Spectroscopy Analysis

The FTIR spectra of Ag–Zn bimetallic nanoparticles and lysine-functionalized Ag–Zn bimetallic nanoparticles confirm the successful synthesis and surface modification of the nanomaterials. In the Ag–Zn bimetallic nanoparticles (Figure 4A), the broad absorption band at 3420 cm^{-1} is attributed to O–H stretching vibrations of adsorbed water and hydroxyl groups, while the peak at 2920 cm^{-1} corresponds to C–H stretching vibrations of residual organic stabilizing agents. The bands observed at 1635 cm^{-1} and 1385 cm^{-1} are assigned to H–O–H bending vibrations of adsorbed water and NO_3^- stretching vibrations originating from residual nitrate precursors, respectively. The peak at 1045 cm^{-1} is associated with C–O stretching vibrations of biomolecules, whereas the bands at 620 cm^{-1} and 470 cm^{-1} correspond to Zn–O and Ag–O/Ag–Zn metal–oxygen vibrations, confirming the formation of the bimetallic framework. Following lysine functionalization (Figure B), characteristic lysine-related bands appear, including O–H/N–H stretching at 3392 cm^{-1}, asymmetric and symmetric $–CH_2–$ stretching vibrations at 2931 cm^{-1} and 2850 cm^{-1}, respectively, COO^- asymmetric and symmetric stretching vibrations at 1610 cm^{-1} and 1402 cm^{-1}, N–H bending at 1536 cm^{-1}, and C–N stretching at 1085 cm^{-1}. The persistence of Zn–O (602 cm^{-1}) and Ag–O/Ag–Zn (470 cm^{-1}) bands together with the emergence of amino acid functional group vibrations confirms the successful attachment of lysine onto the Ag–Zn nanoparticle surface, enhancing nanoparticle stability and biocompatibility.

(A)

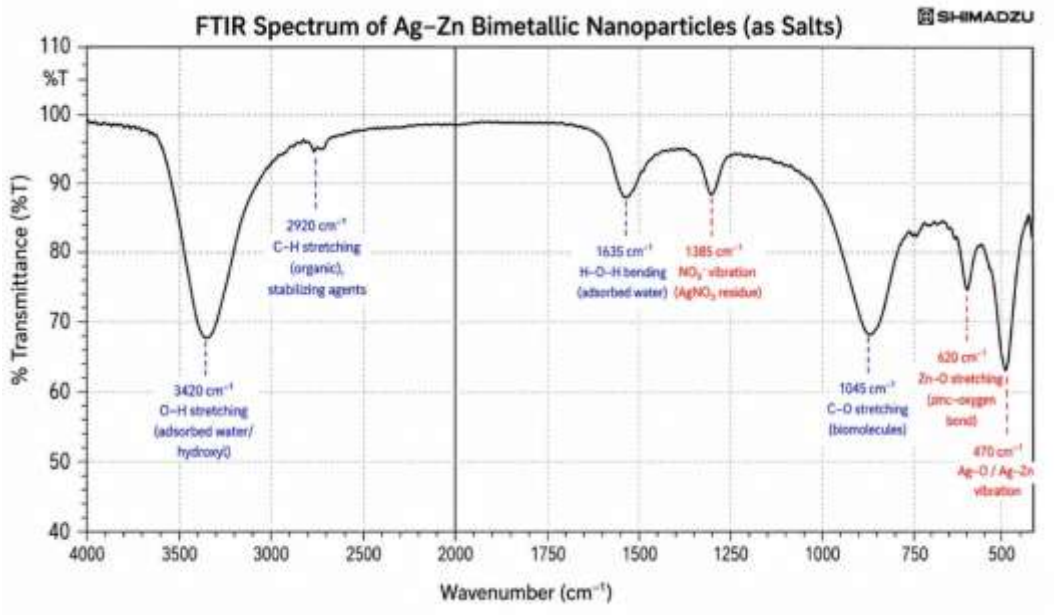

(B)

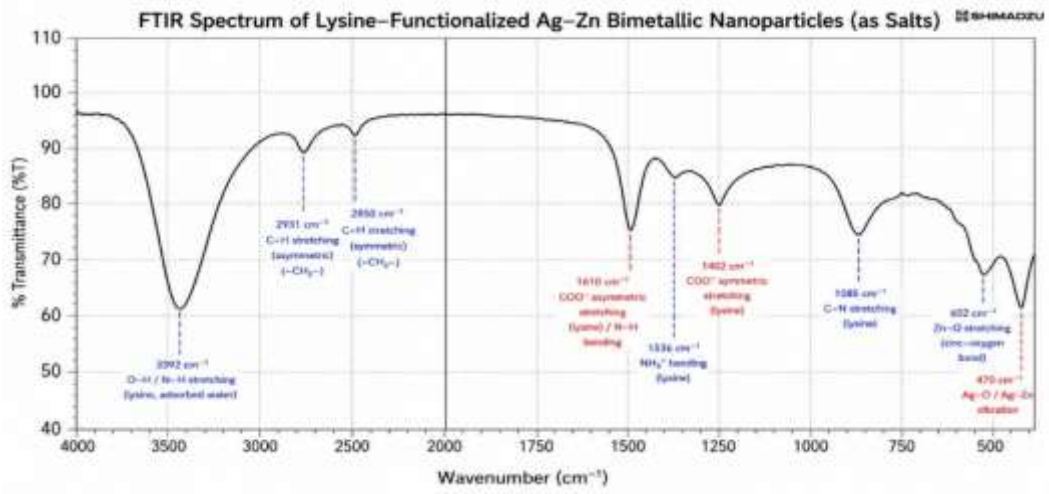

Figure 4. FTIR spectra of (A) Ag–Zn bimetallic nanoparticles and (B) lysine-functionalized Ag–Zn bimetallic nanoparticles. The appearance of characteristic amino (N–H), carboxylate (COO^-), and C–N stretching bands in spectrum (B) confirms successful lysine functionalization of the Ag–Zn nanoparticle surface, while the Zn–O and Ag–O/Ag–Zn vibrational bands indicate preservation of the bimetallic nanostructure after functionalization.

Energy-Dispersive X-ray Spectroscopy (EDX) Analysis of Lysine-Functionalized Ag–Zn Bimetallic Nanoparticles

Energy-dispersive X-ray spectroscopy (EDX) was performed to determine the elemental composition of the synthesized lysine-functionalized Ag–Zn bimetallic nanoparticles. The EDX spectrum exhibited characteristic peaks corresponding to silver (Ag) and zinc (Zn), confirming the successful formation of the Ag–Zn bimetallic nanostructure. The prominent Ag L peak observed at approximately 3.0 keV and the Zn K peak around 8.6–9.6 keV are consistent with the characteristic X-ray emissions of silver and zinc, respectively. In addition, signals corresponding to carbon (C), nitrogen (N), and oxygen (O) were detected at lower energy regions. The presence of carbon and nitrogen is attributed to lysine molecules attached to the nanoparticle surface, while oxygen may originate from surface oxide species, adsorbed moisture, and functional groups present in lysine. The detection of C, N, and O together with Ag and Zn provides strong evidence for successful surface functionalization of the bimetallic nanoparticles with lysine. Furthermore, the absence of significant impurity peaks indicates the high purity of the synthesized nanomaterial. These findings corroborate the FTIR results, confirming the successful incorporation of lysine onto the Ag–Zn nanoparticle surface and the formation of stable lysine-functionalized Ag–Zn bimetallic nanoparticles.

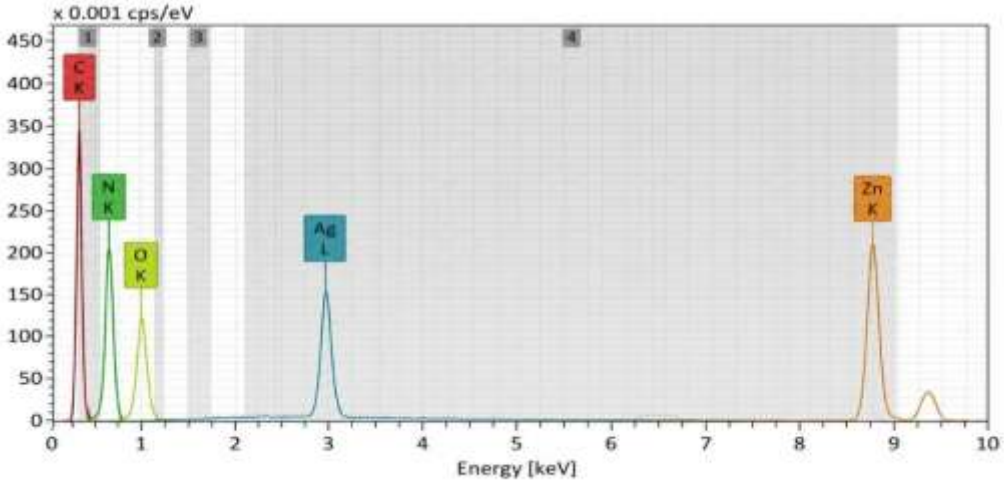

Figure 5. Energy-dispersive X-ray spectroscopy (EDX) spectrum of lysine-functionalized Ag–Zn bimetallic nanoparticles.

Dyes Degradation Activity

The dye degradation efficiency of ZnO–Ag nanoparticles (ZnO–Ag NPs) and lysine-functionalized ZnO–Ag nanoparticles (Lys–ZnO–Ag NPs) was evaluated at different nanoparticle concentrations ranging from 10 to 50 µg/mL. As shown in Figure 6, both nanoparticle formulations exhibited concentration-dependent degradation of the dye, with degradation efficiency increasing as the nanoparticle concentration increased. ZnO–Ag NPs demonstrated degradation efficiencies of 45%, 54%, 66%, 79%, and 92% at concentrations of 10, 20, 30, 40, and 50 µg/mL, respectively. In comparison, Lys–ZnO–Ag NPs showed higher degradation efficiencies of 60%, 73%, 83%, 89%, and 95% at the corresponding concentrations. The enhanced degradation performance of Lys–ZnO–Ag NPs may be attributed to the presence of lysine functional groups on the nanoparticle surface, which improve particle stability, dispersion, and interaction with dye molecules, thereby facilitating more efficient catalytic degradation. The highest degradation efficiencies were observed at 50 µg/mL, where Lys–ZnO–Ag NPs achieved 95% degradation compared to 92% for ZnO–Ag NPs. These findings indicate that lysine functionalization significantly improves the dye degradation capability of Ag–ZnO nanoparticles and highlights their potential application in wastewater treatment and environmental remediation.

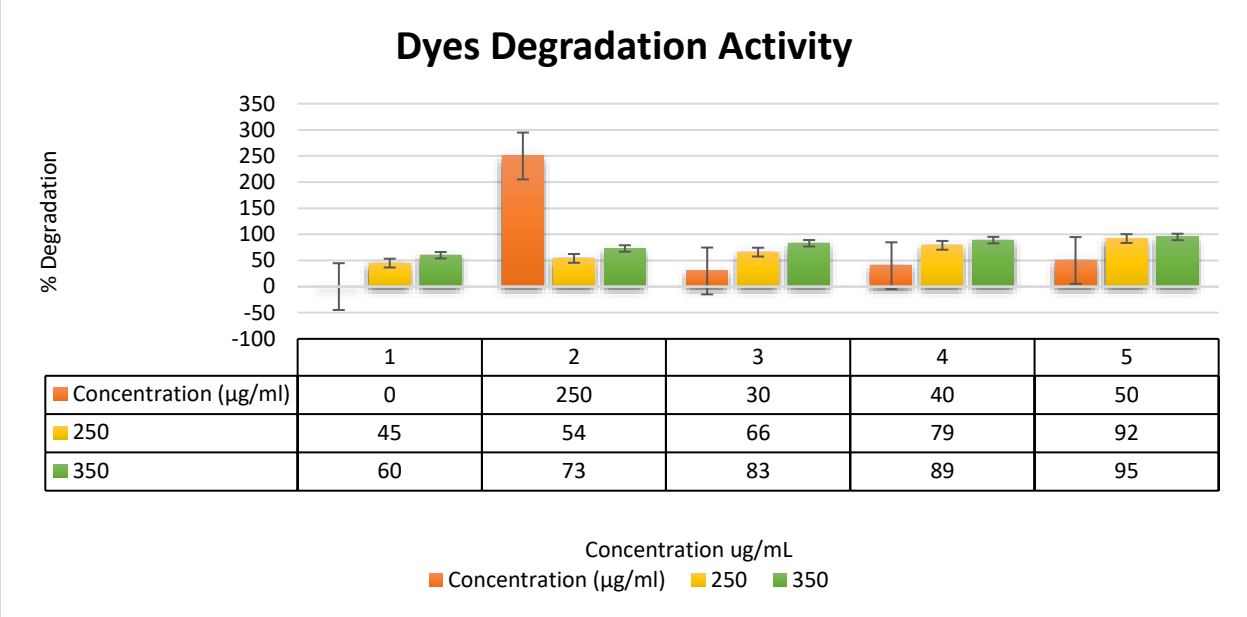

Figure 6. Dye degradation activity of ZnO–Ag nanoparticles (ZnO–Ag NPs) and lysine-functionalized ZnO–Ag nanoparticles (Lys–ZnO–Ag NPs) at different concentrations (10–50 µg/mL). Both nanoparticle formulations exhibited concentration-dependent degradation efficiency, with Lys–ZnO–Ag NPs showing consistently higher degradation performance than ZnO–Ag NPs. Maximum degradation efficiencies of 92% and 95% were achieved by ZnO–Ag NPs and Lys–ZnO–Ag NPs, respectively, at a concentration of 50 µg/mL.

BIOLOGICAL ACTIVITIES

Anti-inflammatory Activity

The anti-inflammatory potential of ZnO nanoparticles (ZnO NPs), Ag nanoparticles (Ag NPs), and lysine-functionalized Ag–ZnO nanoparticles (Lys–Ag–ZnO NPs) was assessed by measuring the inhibition of protein denaturation at different concentrations (150–550 µg/mL). As illustrated in Figure 7, all tested samples exhibited concentration-dependent anti-inflammatory activity, with increasing inhibition percentages observed at higher concentrations. The control group showed inhibition values ranging from 40.2% to 61%, while ZnO NPs demonstrated enhanced activity, reaching 66% inhibition at 550 µg/mL. Ag NPs exhibited greater anti-inflammatory effects, increasing from 49% to 70% across the tested concentration range. Notably, Lys–Ag–ZnO NPs displayed the highest activity, achieving 82.3% inhibition at 550 µg/mL. The improved anti-inflammatory response of the functionalized nanoparticles may be attributed to the synergistic effects of silver and zinc oxide combined with lysine surface modification, which enhances nanoparticle stability and interaction with inflammatory mediators. These findings indicate that lysine functionalization significantly improves the anti-inflammatory efficacy of Ag–ZnO nanoparticles.

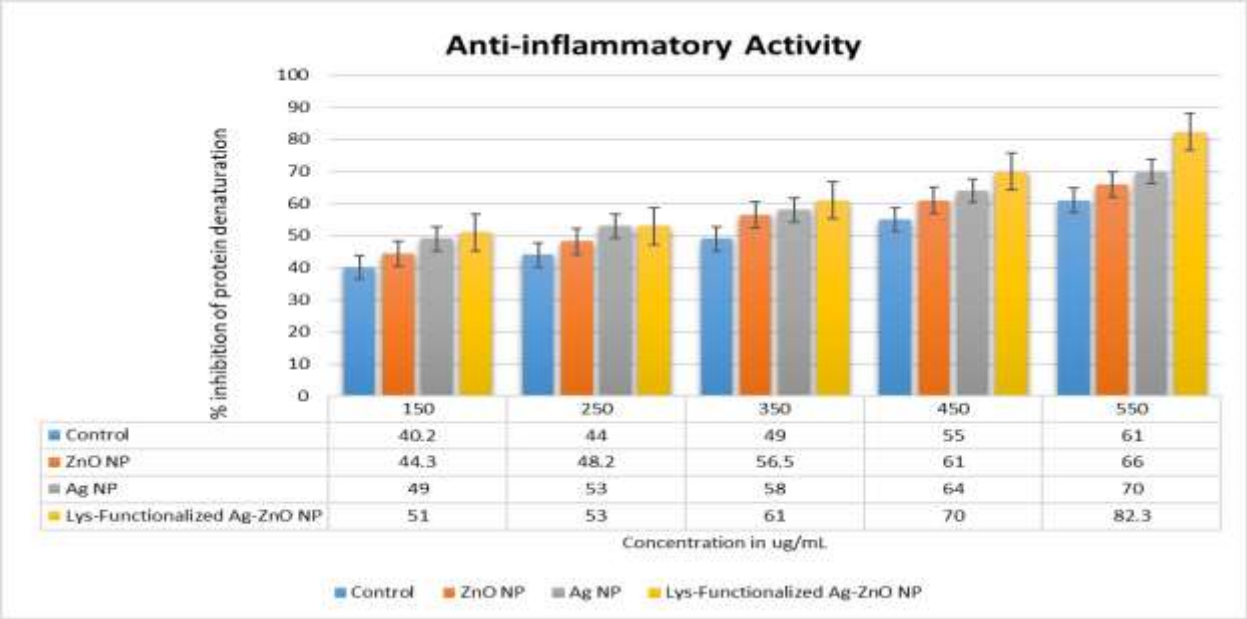

Figure 7. Anti-inflammatory activity of ZnO NPs, Ag NPs, and lysine-functionalized Ag–ZnO NPs evaluated by protein denaturation inhibition assay at different concentrations. Lys–Ag–ZnO NPs exhibited the highest inhibition of protein denaturation, reaching 82.3% at 550 µg/mL, indicating enhanced anti-inflammatory potential compared with non-functionalized nanoparticles.

Anti-oxidant Activity

The antioxidant activity of ZnO NPs, Ag NPs, and Lys–Ag–ZnO NPs was evaluated using the DPPH free radical scavenging assay at concentrations ranging from 100 to 500 µg/mL. As shown in Figure 8, radical scavenging activity increased progressively with increasing nanoparticle concentration for all samples. The control exhibited antioxidant activities between 30% and 57%, whereas ZnO NPs showed improved scavenging activity, reaching 68% at 500 µg/mL. Ag NPs demonstrated stronger antioxidant potential, with values increasing from 42% to 75% across the tested concentrations. Among all formulations, Lys–Ag–ZnO NPs showed the highest antioxidant activity, increasing from 54% at 100 µg/mL to 88.2% at 500 µg/mL. The enhanced radical scavenging ability of the lysine-functionalized nanoparticles may be associated with improved surface properties and increased availability of active sites capable of neutralizing free radicals. These results suggest that lysine functionalization significantly enhances the antioxidant performance of Ag–ZnO nanoparticles.

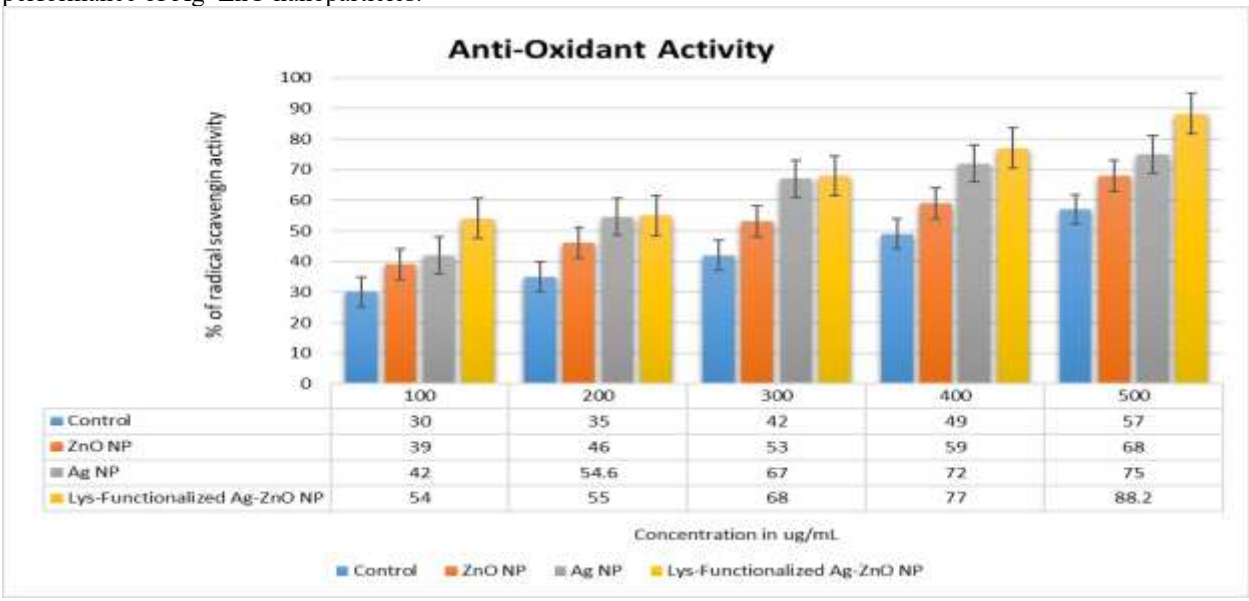

Figure 8. Antioxidant activity of ZnO NPs, Ag NPs, and lysine-functionalized Ag–ZnO NPs determined by the DPPH radical scavenging assay. The scavenging activity increased with concentration, with Lys–Ag–ZnO NPs exhibiting the highest antioxidant activity (88.2%) at 500 µg/mL.

Anti-hemolytic Activity

The anti-hemolytic activity of ZnO NPs, Ag NPs, and Lys–Ag–ZnO NPs was investigated to evaluate their protective effects against red blood cell membrane damage. The results presented in Figure 9 demonstrate a concentration-dependent increase in anti-hemolytic activity for all nanoparticle formulations. The control group showed values ranging from 35% to 67%, while ZnO NPs exhibited anti-hemolytic activity between 53.3% and 70%. Ag NPs demonstrated greater protective effects, increasing from 57.5% at 100 µg/mL to 89% at 500 µg/mL. The highest anti-hemolytic activity was observed for Lys–Ag–ZnO NPs, which increased from 57% at 100 µg/mL to 93.4% at 500 µg/mL. The superior performance of the lysine-functionalized nanoparticles may be attributed to enhanced biocompatibility and stabilization of the nanoparticle surface by lysine molecules, which reduce membrane damage and improve cellular protection. These findings indicate that Lys–Ag–ZnO NPs possess excellent hemocompatibility and may be suitable for biomedical applications.

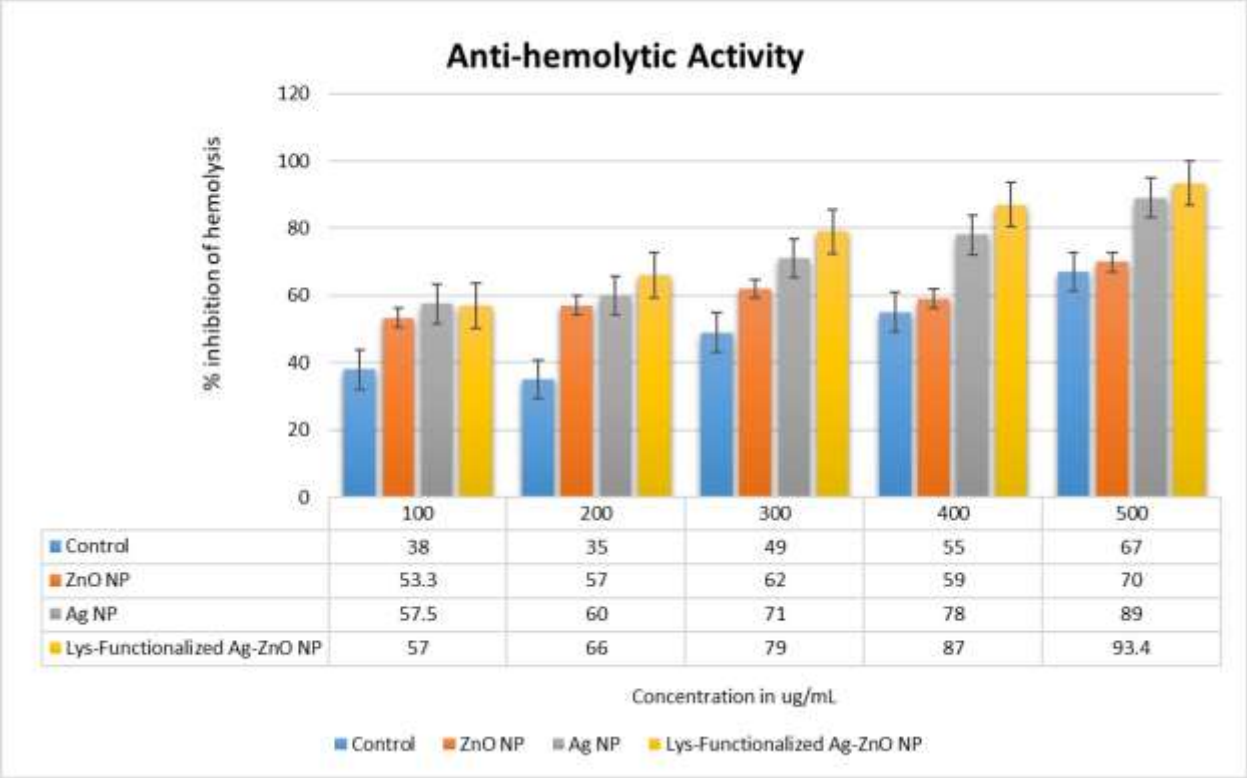

	100	200	300	400	500
Control	38	35	49	55	67
ZnO NP	53.3	57	62	59	70
Ag NP	57.5	60	71	78	89
Lys-Functionalized Ag-ZnO NP	57	66	79	87	93.4

Figure 9. Anti-hemolytic activity of ZnO NPs, Ag NPs, and lysine-functionalized Ag–ZnO NPs at different concentrations. Lys–Ag–ZnO NPs showed the highest protective effect against hemolysis, reaching 93.4% at 500 µg/mL, demonstrating enhanced biocompatibility and hemocompatibility compared with non-functionalized nanoparticles.

DISCUSSION

The present study successfully demonstrated the green synthesis of Ag–ZnO bimetallic nanoparticles using bacterial metabolites and their subsequent functionalization with L-lysine. The combined characterization and biological analyses confirmed that lysine functionalization significantly improved the physicochemical properties, dye degradation efficiency, and biological performance of the synthesized nanoparticles.

UV–Visible spectroscopy provided the first evidence of successful nanoparticle formation and surface modification. The unfunctionalized Ag–ZnO nanoparticles exhibited characteristic absorption bands at 225, 275, and 405 nm, whereas lysine-functionalized nanoparticles showed spectral shifts to 235, 278, and 398 nm. These changes indicate alterations in the local electronic environment surrounding the nanoparticle surface following lysine conjugation. Similar shifts have been reported for amino acid-functionalized metallic nanoparticles, where surface-bound amino

groups modify the dielectric environment and influence surface plasmon resonance behavior. The observed decrease in absorbance intensity and plasmon peak shift suggests successful adsorption of lysine molecules onto the nanoparticle surface, leading to enhanced colloidal stabilization and reduced aggregation [21].

SEM analysis further confirmed the impact of lysine functionalization on nanoparticle morphology. The Ag–ZnO nanoparticles displayed dispersed particles with an average size of approximately 74 nm, while lysine-functionalized nanoparticles exhibited a denser and more uniform morphology with an average size of approximately 82 nm [22]. The increase in particle size following functionalization is expected because lysine molecules form an organic coating around the metallic core. Similar increases in particle diameter after amino acid functionalization have been reported in previous studies involving lysine- and cysteine-modified metal nanoparticles. The relatively narrow size range observed in the present work suggests that bacterial metabolites acted as efficient reducing and stabilizing agents during nanoparticle synthesis. The particle sizes obtained are also within the range commonly reported for biosynthesized Ag–ZnO nanomaterials intended for catalytic and biomedical applications [23].

FTIR analysis provided molecular-level confirmation of nanoparticle synthesis and lysine conjugation. In the unfunctionalized nanoparticles, the bands observed at 3420 cm^{-1}, 2920 cm^{-1}, 1635 cm^{-1}, 1385 cm^{-1}, 1045 cm^{-1}, 620 cm^{-1}, and 470 cm^{-1} corresponded to hydroxyl, organic, nitrate, biomolecular, and metal–oxygen vibrations. Following lysine functionalization, new characteristic bands appeared at 3392 cm^{-1}, 2931 cm^{-1}, 2850 cm^{-1}, 1610 cm^{-1}, 1536 cm^{-1}, 1402 cm^{-1}, and 1085 cm^{-1}, corresponding to amino acid-associated O–H/N–H, CH_2, COO^-, NH_3^+, and C–N functional groups. The persistence of Zn–O and Ag–O/Ag–Zn bands together with the emergence of lysine-specific signals confirms successful attachment of lysine without disrupting the underlying bimetallic structure. Similar FTIR profiles have been reported for amino acid-functionalized metallic nanoparticles where amino and carboxyl groups participate in surface binding and stabilization.

The EDX spectrum further validated successful nanoparticle formation by revealing characteristic elemental signals corresponding to Ag and Zn. The additional presence of carbon, nitrogen, and oxygen in the functionalized sample strongly supports lysine conjugation because these elements are major constituents of amino acid molecules. The absence of significant impurity peaks indicates high nanoparticle purity and suggests that the washing procedures effectively removed unreacted precursors [24]. The combined FTIR and EDX results therefore provide strong evidence that lysine molecules were successfully immobilized on the nanoparticle surface.

One of the most significant findings of this study was the excellent dye degradation performance of the synthesized nanoparticles. Both Ag–ZnO and lysine-functionalized Ag–ZnO nanoparticles exhibited concentration-dependent degradation activity, with degradation efficiencies increasing steadily as nanoparticle concentration increased. The unfunctionalized nanoparticles achieved a maximum degradation efficiency of 92%, whereas lysine-functionalized nanoparticles reached 95% degradation at 50 μg/mL. These values compare favorably with many previously reported biosynthesized metallic nanoparticles, which typically achieve degradation efficiencies ranging from 70–90% under similar conditions. The enhanced degradation efficiency observed after lysine functionalization may be attributed to several factors, including improved nanoparticle dispersion, increased surface area accessibility, and enhanced adsorption of dye molecules through electrostatic interactions between amino groups and dye molecules. Since methylene blue and methyl orange possess different charge characteristics, the presence of lysine may facilitate stronger interactions with both dye species, thereby improving degradation efficiency. Furthermore, the synergistic interaction between silver and zinc oxide likely promotes reactive oxygen species generation, accelerating oxidative breakdown of dye molecules. These findings demonstrate the potential of lysine-functionalized Ag–ZnO nanoparticles as efficient catalysts for wastewater remediation.

The anti-inflammatory assay revealed that all nanoparticle formulations exhibited concentration-dependent inhibition of protein denaturation. Lys–Ag–ZnO nanoparticles showed the highest activity, reaching 82.3% inhibition at 550 μg/mL compared with 70% for Ag nanoparticles and 66% for ZnO nanoparticles. Protein denaturation is a well-recognized mechanism associated with inflammatory disorders, and inhibition of denaturation reflects anti-inflammatory potential [25]. The superior activity of lysine-functionalized nanoparticles may be attributed to enhanced interaction between nanoparticle surfaces and denatured proteins. Moreover, silver and zinc ions are known to modulate inflammatory pathways and reduce oxidative stress. The lysine coating likely contributes additional stabilization and biocompatibility, resulting in improved biological activity. Comparable anti-inflammatory activities have been reported for amino acid-coated metal nanoparticles, supporting the hypothesis that surface functionalization enhances biological interactions and therapeutic potential.

The antioxidant activity results further support the beneficial role of lysine functionalization. Lys–Ag–ZnO nanoparticles exhibited the highest DPPH radical scavenging activity, reaching 88.2% at 500 μg/mL, compared with 75% for Ag nanoparticles and 68% for ZnO nanoparticles. The concentration-dependent increase in radical scavenging activity indicates efficient electron donation and free radical neutralization by the nanoparticle formulations. Similar antioxidant behavior has been reported for biosynthesized metallic nanoparticles, where phytochemicals or biological

capping agents contribute to radical scavenging mechanisms [26]. In the present study, bacterial metabolites and lysine molecules likely acted synergistically with the metallic core to enhance electron transfer processes. The amino and carboxyl groups of lysine may also facilitate hydrogen atom donation, thereby improving antioxidant efficiency. The obtained antioxidant values are comparatively high and demonstrate the effectiveness of amino acid functionalization in enhancing the free radical scavenging capacity of bimetallic nanoparticles.

Biocompatibility assessment through the anti-hemolytic assay demonstrated excellent protective effects against red blood cell membrane damage. Lys–Ag–ZnO nanoparticles achieved 93.4% protection at 500 µg/mL, outperforming Ag nanoparticles (89%) and ZnO nanoparticles (70%). Hemocompatibility is an important consideration for biomedical applications because direct interactions between nanoparticles and blood components can influence safety and therapeutic effectiveness. The enhanced anti-hemolytic activity observed for lysine-functionalized nanoparticles may be attributed to the formation of a biocompatible amino acid shell around the nanoparticle surface, reducing direct membrane disruption and minimizing oxidative damage. Similar improvements in hemocompatibility have been reported following amino acid and polymer functionalization of metallic nanoparticles. The high anti-hemolytic activity observed in the present study suggests that lysine functionalization substantially improves nanoparticle safety and suitability for future biomedical applications.

Overall, the results clearly demonstrate that lysine functionalization enhanced nearly every evaluated parameter, including colloidal stability, dye degradation efficiency, antioxidant activity, anti-inflammatory activity, and hemocompatibility. The synergistic combination of bacterial metabolite-mediated green synthesis, Ag–ZnO bimetallic architecture, and lysine surface functionalization produced nanoparticles with superior environmental and biological performance. These findings highlight the potential application of lysine-functionalized Ag–ZnO nanoparticles in wastewater treatment, environmental remediation, antioxidant therapies, anti-inflammatory interventions, and other biomedical applications.

REFERENCES

1. Kamankesh, M., Yadegar, A., Llopis-Lorente, A., Liu, C., Haririan, I., Aghdaei, H. A., ... & Wacker, M. G. (2024). Future nanotechnology-based strategies for improved management of Helicobacter pylori infection. Small, 20(3), 2302532.
2. Idris, D. S., & Roy, A. (2023). Synthesis of bimetallic nanoparticles and applications—an updated review. Crystals, 13(4), 637.
3. Islam, M. T., Islam, T., Islam, T., & Repon, M. R. (2022). Synthetic dyes for textile colouration: Process, factors and environmental impact. Textile and leather review., 5, 327-373.
4. Oladoye, P. O., Ajiboye, T. O., Omotola, E. O., & Oyewola, O. J. (2022). Methylene blue dye: Toxicity and potential elimination technology from wastewater. Results in Engineering, 16, 100678.
5. Sangamnere, R., Misra, T., Bherwani, H., Kapley, A., & Kumar, R. (2023). A critical review of conventional and emerging wastewater treatment technologies. Sustainable Water Resources Management, 9(2), 58.
6. Wang, S., Liu, H., Wu, Q., Shu, Y., Wang, Q., Zhang, G., ... & Liang, F. (2024). Catalytic Janus nanoparticle-based recyclable emulsifiers for collaborative treatment of water-soluble and water-insoluble organic pollutants. ACS Applied Nano Materials, 7(12), 14820-14828.
7. Mayegowda, S. B., Sarma, G., Gadilingappa, M. N., Alghamdi, S., Aslam, A., Refaat, B., ... & Al-Moraya, I. S. (2023). Green-synthesized nanoparticles and their therapeutic applications: A review. Green Processing and Synthesis, 12(1), 20230001.
8. Ahmad, F., Salem-Bekhit, M. M., Khan, F., Alshehri, S., Khan, A., Ghoneim, M. M., ... & Elbagory, I. (2022). Unique properties of surface-functionalized nanoparticles for bio-application: functionalization mechanisms and importance in application. Nanomaterials, 12(8), 1333.
9. Rafeeq, H., Hussain, A., Ambreen, A., Waqas, M., Bilal, M., & Iqbal, H. M. (2022). Functionalized nanoparticles and their environmental remediation potential: a review. Journal of Nanostructure in Chemistry, 12(6), 1007-1031.
10. Asim, M., Naveed, M., Aziz, T., Din, M. S. U., Alshehri, F., Shami, A., ... & Al-Joufi, F. A. (2025). Artificial neural network optimized green synthesis of cysteine-conjugated silver nanoparticles for antibacterial activity against staphylococcus nepalensis to combat cystitis. Antonie van Leeuwenhoek, 118(11), 166.
11. Kaveh, M., & Mesgari, M. S. (2022). Application of meta-heuristic algorithms for training neural networks and deep learning architectures: A comprehensive review. Neural Processing Letters, 1.
12. Arslan, N. P., Azad, F., Orak, T., Budak-Savas, A., Ortucu, S., Dawar, P., ... & Taskin, M. (2025). A review on bacteria-derived antioxidant metabolites: their production, purification, characterization, potential applications, and limitations. Archives of Pharmacal Research, 48(4), 253.

13. Naveed, M., Din, M. S. U., Aziz, T., Asim, M., Makhdoom, S. I., Khan, A. A., ... & Alrayyani, M. A. (2025). Biosynthesis of cysteine-conjugated zinc oxide nanoparticles using secondary metabolites of Bacillus licheniformis for wastewater purification. Desalination and Water Treatment, 101370.
14. Shi, Z., Chow, C. W., Fabris, R., Liu, J., & Jin, B. (2022). Applications of online UV-Vis spectrophotometer for drinking water quality monitoring and process control: a review. Sensors, 22(8), 2987.
15. Vijayaram, S., Razafindralambo, H., Sun, Y. Z., Vasantharaj, S., Ghafarifarsani, H., Hoseinifar, S. H., & Raeeszadeh, M. (2023). Applications of green synthesized metal nanoparticles—a review. Biological trace element research, 1.
16. Eid, M. M. (2022). Characterization of Nanoparticles by FTIR and FTIR-Microscopy. In Handbook of consumer nanoproducts (pp. 1-30). Singapore: Springer Singapore.
17. Naveed, M., Asim, M., Aziz, T., Ibrahim, S., Din, M. S. U., Alomran, M. M., ... & Alhomrani, M. (2025). Molecular characterization and green synthesis of iron oxide nanoparticles from Ureibacillus chungkukjangi for methylene blue degradation. Antonie van Leeuwenhoek, 118(10), 149.
18. Din, M. S. U., Naveed, M., Aziz, T., Makhdoom, S. I., Waseem, M., Khan, A. A., ... & Alasmari, A. F. (2025). Comprehensive characterization and bioactivity assessment of titanium dioxide nanoparticles synthesized using Chrysanthemum indicum leaf extract. Chemistry & Biodiversity, 22(6), e202500244.
19. Naveed, M., Asim, M., Aziz, T., Nasir, S., Din, M. S. U., Al-Hoshani, N., ... & Al-Joufi, F. A. (2026). Biosynthesis and Biological Assessment of TiO_2 Nanoparticles from Pittosporum Tobira for Antioxidant, Anti-Inflammatory, Anti-Hemolytic Potential, and Polychlorinated Biphenyls Degradation. Water, Air, & Soil Pollution, 237(6), 343.
20. Ben Amor, A., Hemmami, H., Gherbi, M. T., Seghir, B. B., Zeghoud, S., Gharbi, A. H., ... & Barhoum, A. (2025). Synthesis of spherical carbon nanoparticles from orange peel and their surface modification with chitosan: Evaluation of optical properties, biocompatibility, antioxidant and anti-hemolytic activity. Biomass Conversion and Biorefinery, 15(7), 11345-11358.
21. Idris, D. S., Roy, A., Subramanian, A., Alghamdi, S., Chidamabaram, K., & Qusty, N. F. (2024). Bio-fabrication of silver–zinc bimetallic nanoparticles and its antibacterial and dye degradation activity. Journal of Inorganic and Organometallic Polymers and Materials, 34(5), 1908-1919.
22. Ehsan, M., Waheed, A., Ullah, A., Kazmi, A., Ali, A., Raja, N. I., ... & Li, H. (2022). Plant-based bimetallic silver-zinc oxide nanoparticles: A comprehensive perspective of synthesis, biomedical applications, and future trends. BioMed research international, 2022(1), 1215183.
23. Chrószcz-Porębska, M., & Gadomska-Gajadhur, A. (2024). Cysteine conjugation: an approach to obtain polymers with enhanced muco-and tissue adhesion. International Journal of Molecular Sciences, 25(22), 12177.
24. Shrestha, D. K., Magar, A. B., Bhusal, M., Baraili, R., Pathak, I., Joshi, P. R., ... & Sharma, K. R. (2024). Synthesis of silver and zinc oxide nanoparticles using Polystichum lentum extract for the potential antibacterial, antioxidant, and anticancer activities. Journal of Chemistry, 2024(1), 1876560.
25. Corsi, F., Deidda Tarquini, G., Urbani, M., Bejarano, I., Traversa, E., & Ghibelli, L. (2023). The impressive anti-inflammatory activity of cerium oxide nanoparticles: more than redox?. Nanomaterials, 13(20), 2803.
26. Daré, R. G., & Lautenschlager, S. O. (2025). Nanoparticles with antioxidant activity. Antioxidants, 14(2), 221.